Structure and variability of Langmuir circulation during the Surface Waves Processes Program

Albert J. Plueddemann,[1] Jerome A. Smith,[2] David M. Farmer,[3] Robert A. Weller,[1] William R. Crawford,[3] Robert Pinkel,[2] Svein Vagle,[3] and Anand Gnanadesikan[1]

Abstract. A cooperative, multiplatform field experiment was conducted in the eastern North Pacific during February and March of 1990 as part of the Surface Waves Processes Program (SWAPP). One of the experimental objectives was to investigate Langmuir circulation so that its role in the evolution of the oceanic surface boundary layer could be better understood. The concurrent use of different observational techniques, ranging from simple surface drifters to complex Doppler sonar systems, resulted in new information about Langmuir circulation structure and variability. Estimates of Langmuir cell spacing indicated that a broad range of scales, from about 2 to 200 m, was excited during periods of strong surface forcing and that the energy containing scales evolved with time. Estimates of cell spacing based on Doppler velocities from a surface-scanning sonar directed crosswind showed this scale evolution, but estimates based on backscattered intensity did not. This was attributed to the fact that the intensity-based estimates were only indirectly related to circulation strength. The near-surface convergent velocities from the sonar were used to form an objective, quantitative measure of the temporal variations in Langmuir circulation strength. As expected, the circulation strength increased dramatically during strong wind events. However, circulation strength and wind stress did not decrease simultaneously, and Langmuir circulation was detectable for up to a day after abrupt reductions in wind stress. Energy from the surface wave field, which decayed more slowly than the wind, was apparently responsible for maintaining the circulation. The variation of circulation strength was found to be better related to $(u_* U_s)^{1/2}$ than to u_*, where $u_* = (\tau/\rho)^{1/2}$ is the friction velocity, τ is the wind stress, and U_s is the surface wave Stokes drift. This scaling is consistent with wave-current interaction theories of Langmuir cell generation.

1. Introduction

This paper reports a set of coordinated observations of Langmuir circulation in the open ocean using a variety of measurement techniques, ranging from computer cards, used as surface drifters in the tradition of the original observations of Langmuir [1938], to Doppler sonars which imaged the surface of the sea from below. The data were collected as part of the Surface Wave Processes Program (SWAPP) [Weller et al., 1991]. The SWAPP field experiment was conducted at a site about 550 km west of Point Conception, California, during a 23-day period from February 24 to March 18, 1990.

[1] Department of Physical Oceanography, Woods Hole Oceanographic Institution, Woods Hole, Massachusetts.
[2] Scripps Institution of Oceanography, La Jolla, California.
[3] Institute of Ocean Sciences, Sidney, British Columbia, Canada.

The central platforms of SWAPP were the R/P *Flip* of the Scripps Institution of Oceanography (SIO) and the C.S.S. *Parizeau* of the Institute of Ocean Sciences (IOS), Canada. *Flip* was towed to the experimental site and fixed on station at 35.137°N, 126.984°W on February 21 using a three-point mooring. Instrumentation deployed from *Flip* included a multibeam sonar system, meteorological sensors, capacitance and resistance wave staffs, profiling conductivity-temperature-depth (CTD) instruments, and two vertical arrays of current meters. The *Parizeau* arrived on station on February 25 and worked in near proximity to *Flip*. Typical operations from *Parizeau* involved deployment and recovery of a drifting sonar system, deployment of a free-fall microstructure probe, and deployment and recovery of the 5-m launch *Slicker* which was used for turbulence profiling when conditions were favorable. A general description of the experimental plan is given by *Weller et al.* [1991]. Measurement techniques relevant to the detection of Langmuir circulation are described in more detail in section 2.

The location and time of year for the SWAPP experiment were chosen based on the desire to experience a range of wind and wave conditions, including...
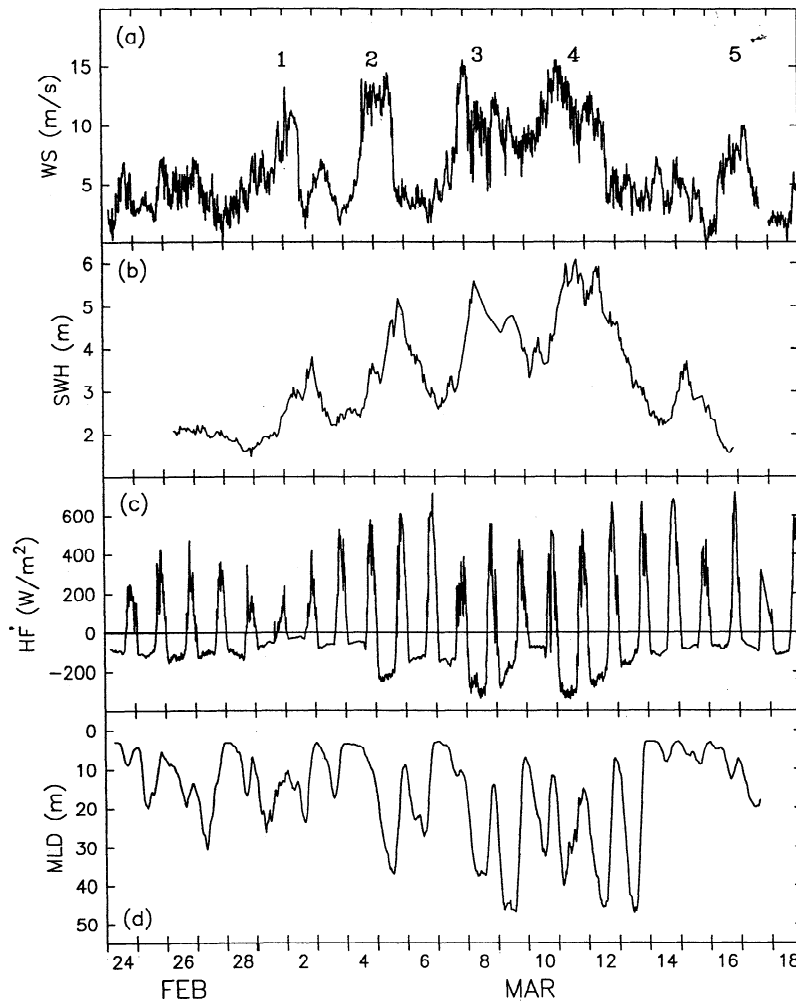
Figure 1. Time series of (a) wind speed, (b) significant wave height, (c) total heat flux, and (d) mixed layer depth observed from R/P *Flip* during the Surface Waves Processes Program (SWAPP). The passage of atmospheric fronts resulted in five distinct "events" at the SWAPP site which are most clearly seen in the wind speed record. Heat flux was computed from 1-min average meteorological variables using stability dependent bulk formulae [*Large and Pond*, 1982]. Wave height was measured with a capacitive wave staff. Mixed layer depth was estimated using a $\Delta T = 0.01°C$ criterion and a reference depth of 2.25 m (*Weller and Plueddemann*, submitted manuscript, 1995).

optic variability in the local meteorology, and to work in a mixed layer of modest depth so that changes in mixed layer structure could be readily observed. The desired conditions were achieved as a series of high- and low-pressure systems passed near the SWAPP site. Figure 1 shows time series of wind stress, significant wave height, total heat flux, and mixed layer depth observed during the experiment. Five distinct forcing "events" identified in the meteorological variables measured from *Flip* (*R. A. Weller and A. J. Plueddemann*, Observations of the vertical structure of the oceanic boundary layer, submitted to *Journal of Geophysical Research*, hereinafter referred to as submitted manuscript, 1995) are labeled in Figure 1. The first and fifth events brought warm, moist air from the south and were not associated with substantial wave growth.

The second, third, and fourth events were characterized by cold, dry winds from the northwest and were associated with substantial increases in significant wave height. The second wind event was the most dramatic, building from 3 to 13 m s^{-1} in about 10 hours with an associated increase in significant wave height from 2.5 to 5 m. The third event showed the highest wind speed (near 16 m s^{-1}), while the largest waves (over 6 m significant wave height) were seen during the fourth event. Note that the decay in significant wave height clearly lagged that of the wind in events 2 and 4. This was the result of swell propagating from the storm centers which were to the west and northwest of the site.

The results described in this paper concentrate on analysis of the sonar data (section 3), with relevant observations from other sensors described briefly

(section 2) and included as a part of the discussion (section 4). Much of what we found was similar to that reported by previous investigators. Acoustic backscatter was dominated by returns from bubble clouds for wind speeds above 3–4 m s^{-1}, and the bubbles formed a nearly continuous layer for speeds above 5–6 m s^{-1} [*Thorpe and Hall*, 1983; *Zedel and Farmer*, 1991]. The penetration depth of bubble plumes seen in vertically oriented sonar beams increased with increasing wind speed [*Thorpe*, 1986]. Bands of enhanced backscatter were seen in surface-scanning sonar records. These bands were oriented approximately downwind, and their properties were consistent with the assumption that they were caused by the collection of bubbles in the convergence zones of Langmuir circulation [*Thorpe and Hall*, 1983; *Thorpe*, 1984; *Smith et al.*, 1987; *Zedel and Farmer*, 1991]. A broad range of convergence zone spacings (2–200 m) were detected simultaneously using a variety of techniques, and the spacing of wind rows formed by surface drifters evolved from the smallest to the largest scales over time [*Katz et al.*, 1965; *Ichiye*, 1967; *Assaf et al.*, 1971; *Weller and Price*, 1988].

However, the results presented here differ from previous work in several respects. Different techniques for observing Langmuir cell structure and variability were employed simultaneously, and the results are compared. Estimates of convergence zone spacing based on backscattered intensity showed variability over a broad range of scales, but a dominant scale was difficult to identify and changes in scale were difficult to determine. In contrast, the Doppler velocity from the surface-scanning sonars showed changes in scale concurrent with variations in surface forcing. Processing techniques were introduced which exploited the two-dimensional (time/range) information contained in the sonar data. One of the results was an objective, quantitative measure of Langmuir circulation strength for a 20-day period spanning several storm events. The circulation strength determined from this and other measures typically increased with increasing wind speed. However, circulation strength did not necessarily decrease with decreasing winds, and in several cases, robust circulation continued to exist long after the wind decayed. This was apparently the result of forcing from surface waves which did not decay as rapidly as the wind. Dissipation measurements were made in the convergence zones of the Langmuir cells, as defined by lines of surface drifters. Contrary to expectations, there was no indication of enhanced dissipation within these zones.

2. Measurement Techniques

2.1. Surface Drifters

Paper computer cards, used by the thousands in the days when computer programs were written on punched cards and submitted as batch jobs, were used as surface drifters in the manner of *Weller and Price* [1988]. Card deployments were made from *Flip* one or more times per day during most of the experimental period. These deployments typically consisted of an initial "seeding" of cards and subsequent "reseeding" as the cards from the initial deployment drifted away from the moored platform. Card deployments from *Parizeau* and *Slicker* were done while the ships steamed slowly in the crosswind direction. In order to make observations at night, when computer cards could not be seen, floating lights fabricated from squares of plywood and saltwater-activated incandescent bulbs were used.

A total of 40 drifter deployments from *Flip* were documented. Quantitative observations from the *Flip* deployments consisted of estimates of alignment time (the interval between deployment of the drifters and their organization into distinct rows) and row spacing (the crosswind distance between rows after alignment). If all of the drifters were captured in a single convergence zone, a spacing of 15 m was assigned, imposing an upper limit to the row spacing. The mobility of *Parizeau* and *Slicker* compared with *Flip* meant that the drifters could be spaced more widely in the crosswind direction and much larger cell spacings could be detected. Row spacing data for 56 deployments were documented by *Crawford* [1992], but alignment times were not recorded.

2.2. Current Meters

Observations of temperature and horizontal velocity in the upper ocean were made using vector-measuring current meters (VMCMs), modified for real-time sampling [*Park et al.*, 1991] and deployed from *Flip*'s booms. A total of 19 VMCMs were deployed in two vertical arrays for investigation of upper ocean structure (*Weller and Plueddemann*, submitted manuscript, 1995). Here we report only the vertical shear between the uppermost instrument locations common to the two arrays: 2.25 and 6.75 m depth. *Weller and Price* [1988] showed that the downwind flow in the convergence zones of Langmuir cells had a subsurface maximum, resulting in a reversal of the vertical shear of horizontal velocity with depth. They also suggested that the time-varying amplitude of near-surface shear could be used as an indicator of Langmuir circulation strength. In the presence of cells aligned approximately downwind and advected crosswind past the current meter arrays, a signal arises in the vertical shear from encounters with convergence zone jets. The frequency of the signal is determined by the cell orientation and spacing, along with the speed and direction of advection past the instruments. Encounter periods could range from about a minute (e.g., cells with 10-m spacing advected crosswind by currents of 20 cm s^{-1}) to arbitrarily long (downwind advection).

Analysis of shear spectra from SWAPP indicated that a frequency band between 1 and 36 cph would be effective in isolating the signal related to Langmuir circulation [*Gnanadesikan*, 1994]. The processing of shear in the 1–36 cph band was complicated by the periodic pres-

ence of a wake from *Flip*'s hull due to lower-frequency, rotational (inertial and tidal) currents. The presence of the wake resulted in sudden increases in shear variability and thus was easily detectable. The two current meter arrays were well separated and the wake affected only one at a time. A single, uncontaminated shear record was created by selecting the value from the wake-free array. Uncertainty in the shear estimate due to instrumental error was estimated to be of order 1×10^{-3} s^{-1} (*Weller and Plueddemann*, submitted manuscript, 1995). Shear bias introduced by the motion of the VMCMs in the wave zone varied with wave height and decreased with depth below the surface. For a significant wave height of 5 m the error in the 2.25 to 6.75-m band-passed shear was of order 4×10^{-4} s^{-1} [*Gnanadesikan*, 1994].

2.3. Microstructure Profiling

Microstructure profiling was carried out both from *Parizeau* and from the launch *Slicker* using a tethered microstructure profiler designated the fast light yoyo (FLY) [*Dewey et al.*, 1987; *Crawford*, 1992]. Sensors on FLY included two airfoil shear probes, a fast response thermistor, a Sea-Bird SBE-4-04/A conductivity cell, two tilt gauges, and a pressure gauge. Here we are concerned with the near-surface (5–40 m depth) profiling work from *Slicker*, which was designed to contrast the turbulence signature inside and outside of Langmuir cell convergence zones. The *Slicker* was not an ideal design for work in rough weather (its flat bottom gave a rough ride in lumpy seas), but its advantages were that it was small enough to be easily handled by *Parizeau* and that it had a draft of only about 10 cm, so it did not disturb the near-surface flow. The shallow draft was critical for making measurements to within a few meters of the surface, but the limitations of the small launch restricted operations to relatively light wind (<10 m s^{-1}) and moderate sea state.

Subject to these limitations, a series of 101 microstructure profiles were done from *Slicker* during the experiment. Two 1× 5 m "holey sock" drogues were tied to the bow to act as sea anchors and the launch allowed to drift with the outboard motor raised out of the water. The profiler was deployed by suspending the probe over the water from a davit, then releasing the probe and paying out the tether at a speed somewhat faster than the fall speed of the probe (nominally, 1 m s^{-1}). Prior to and during profiling operations, computer cards were thrown into the water every 10 min. Even with two sea anchors in the water, the launch drifted downwind faster than the cards and was made to drift across the card rows by tying the anchor line to either the port or starboard side of the launch and letting the windage move her sideways. In this way, microstructure profiles were made at a series of positions relative to the convergence zones of the Langmuir cells.

2.4. Sonar Systems

Two sonar systems were used during SWAPP, one was a self-contained, free-drifting device developed by IOS and the other was deployed and operated by SIO from *Flip*. The appeal of the sonars is their ability to detect coherent features that could be identified with Langmuir circulation [*Thorpe and Hall*, 1983; *Smith et al.*, 1987; *Zedel and Farmer*, 1991; *Smith*, 1992; *Thorpe et al.*, 1994]. Sonar imaging of near-surface circulation patterns results from resonant backscatter from a layer of microbubbles (radius 20–400 μm). The bubbles are presumed to be injected into the surface layer at random locations by breaking waves and then concentrated into "rows" by horizontal convergences and drawn downward into "plumes" by vertical currents. At low wind speeds, microbubbles may exist only in patches or be nonexistent. However, in winds over 3–4 m s^{-1} the bubbles form a nearly continuous near-surface layer which dominates the backscattered signal [*Thorpe*, 1986; *Crawford and Farmer*, 1987]. The backscatter due to bubbles far exceeds that from either the sea surface above or the volume below the bubble layer, effectively restricting the vertical extent of the sonar measurement volume to a 2 to 3-m thick surface layer.

The IOS acoustics drifter "Susy" is described by *Zedel and Farmer* [1991] and *Trevorrow and Teichrob* [1994]. As configured for SWAPP, Susy detected the bubble layer with two different sonar systems, surface-scanning sonars and vertically oriented, narrow beam sonars. These systems were deployed as part of a self-contained, internally recording instrument which was suspended from a surface float at depths ranging from 24 to 40 m. A rubber bungy cord and the added mass of water near upper and lower damper plates effectively restrained the instrument's motion to residual orbital displacements of the swell which were detected with an accelerometer and tiltmeters. Additional sensors, not discussed further here, included an array of broadband hydrophones for studies of the high-frequency sound field generated by breaking surface waves.

The operating parameters for both the surface-scanning and vertical sonar systems are summarized in Table 1. The two orthogonal surface-scanning sonars operated at 100 kHz and were primarily sensitive to bubbles with a radius between 32 and 40 μm. During operation each sonar transmitted a 1-ms duration pulse every 0.5 s, giving a range resolution of 0.74 m over a total range interval of about 250 m. The azimuthal beam width of 2° translated into a cross-beam resolution of about 9 m at 250-m range. The six vertically oriented sonars transmitted at twice the rate of the surface-scanning sonars. By using different frequencies (between 28 and 400 kHz) and short pulse lengths, it was possible to detect the bubble concentration at different resonant radii with a range resolution varying

Table 1. Institute of Ocean Sciences Acoustics Drifter Operating Parameters

	Vertical Sonars	Surface-Scan Sonars
Number of sonars	6	2
Transmit frequencies, kHz	28, 50, 88, 120, 200, 400	100
Resonant bubble radii, μm	121, 68, 38, 28, 17, 8	34
–3dB beamwidths, deg	17, 8, 6, 5, 3, 4	...
–3dB beamwidth, horizontal, deg		2
–3dB beamwidth, vertical, deg		50
Transmit rate, Hz	4	2
Pulse width, ms	0.5–0.6	1.0
Pulse lengths, m	0.37–0.44	0.74
Instrument depth, m	24–40	250

between 0.37 and 0.44 m. Backscatter strengths from the vertical sonars were referenced to the sea surface and corrected for relative motion using the methods described by *Vagle and Farmer* [1992]. Susy was deployed 11 times during SWAPP, with a total recording time of 257 hours. The instrument collected data in two different modes during each deployment. For a given period, only the "passive" broadband hydrophones were operated, followed by a period when the "active" surface-scanning and vertical sonars were used. Only the active data collection periods are discussed here, concentrating on five deployments with wind speed >2 m s^{-1} (Table 2).

Two surface-scanning Doppler sonar systems were deployed on *Flip* for the duration of SWAPP. The configuration and operation of both systems are described by *Smith* [1992]. In this paper we present results from the "high-resolution" system, which consisted of four beams oriented at 45° increments in azimuth [*Smith*, 1992, Figure 3]. The system operated at 195 kHz and achieved horizontal ranges near 400 m. The beam width of the 195-kHz system was 2/3° (azimuth) by 22° (vertical), and the cross-beam resolution was about 3 m at 250-m range. Velocity estimates were made from the time-lagged covariance of the backscattered signal using a repeat-sequence, coded pulse technique [*Pinkel and Smith*, 1991]. A four-bit code was transmitted every 3/4 s. Covariance estimates were averaged in range over about 3 m (4 ms), yielding an estimated rms error of about 10 cm s^{-1} in each range bin per transmission. For most of the experiment, data collection alternated hourly between "wave mode" ($\sim$52-min du-

Table 2. IOS Acoustics Drifter Deployment Summary

	Date and Time, UTC		Symbol in Figure 5
Deployment	Start	End	
5	March 4, 1850	March 5, 1830	square
6	March 8, 0650	March 9, 2330	triangle
7	March 10, 0050	March 10, 2250	diamond
8	March 12, 1844	March 13, 0200	inverted triangle
9	March 14, 0115	March 14, 2130	circle

ration), in which every transmission was recorded and "Langmuir mode" ($\sim$68-min duration), in which 1-min averages were recorded. Recording every transmission allowed surface wave directional spectra to be estimated in the manner described by *Smith* [1989]. The wave mode data were subsequently averaged and combined with the Langmuir mode data, providing a nearly continuous time series of 1-min-averaged data for the duration of the experiment. The rms velocity error in the 1-min data was reduced to about 1 cm s^{-1}.

3. Sonar-Based Observations

3.1. Analysis of Sonar Images

Sonar images from both Susy and *Flip* tracked bubble clouds, which acted as "quasi-Lagrangian" tracers within the flow field associated with Langmuir cells. The intensity from a surface-scanning sonar beam directed approximately crosswind showed the rows of bubble clouds collected in successive convergence zones, while the Doppler velocity showed the alternating convergent and divergent currents associated with the cells. The data from individual sonar beams were displayed as "time-range maps," with backscattered intensity or Doppler velocity contoured on a plane defined by time versus range. There was usually a crosswind component of relative velocity between the sea surface and the instrument, causing the convergence zones to migrate in range with time and resulting in a sequence of lines or "bands" at some angle.

Examples of time-range maps of Doppler velocity obtained from the *Flip* sonars are shown in Figure 2a for a 12-hour period spanning the initiation of the second wind event. Prior to the wind event (1200–1500 UTC, labeled A in Figure 2a) all four beams show a mottled pattern with no identifiable features. With the onset of strong wind at about 1520 UTC (labeled B), small-scale bands are observed which appear to accelerate towards *Flip* in response to changes in the advection velocity. The wind speed continued to increase from 1600 to 1900 UTC, eventually stabilizing at about 13 m s^{-1}. During this period the bands grow in scale and increase in strength. The most well-developed features are seen
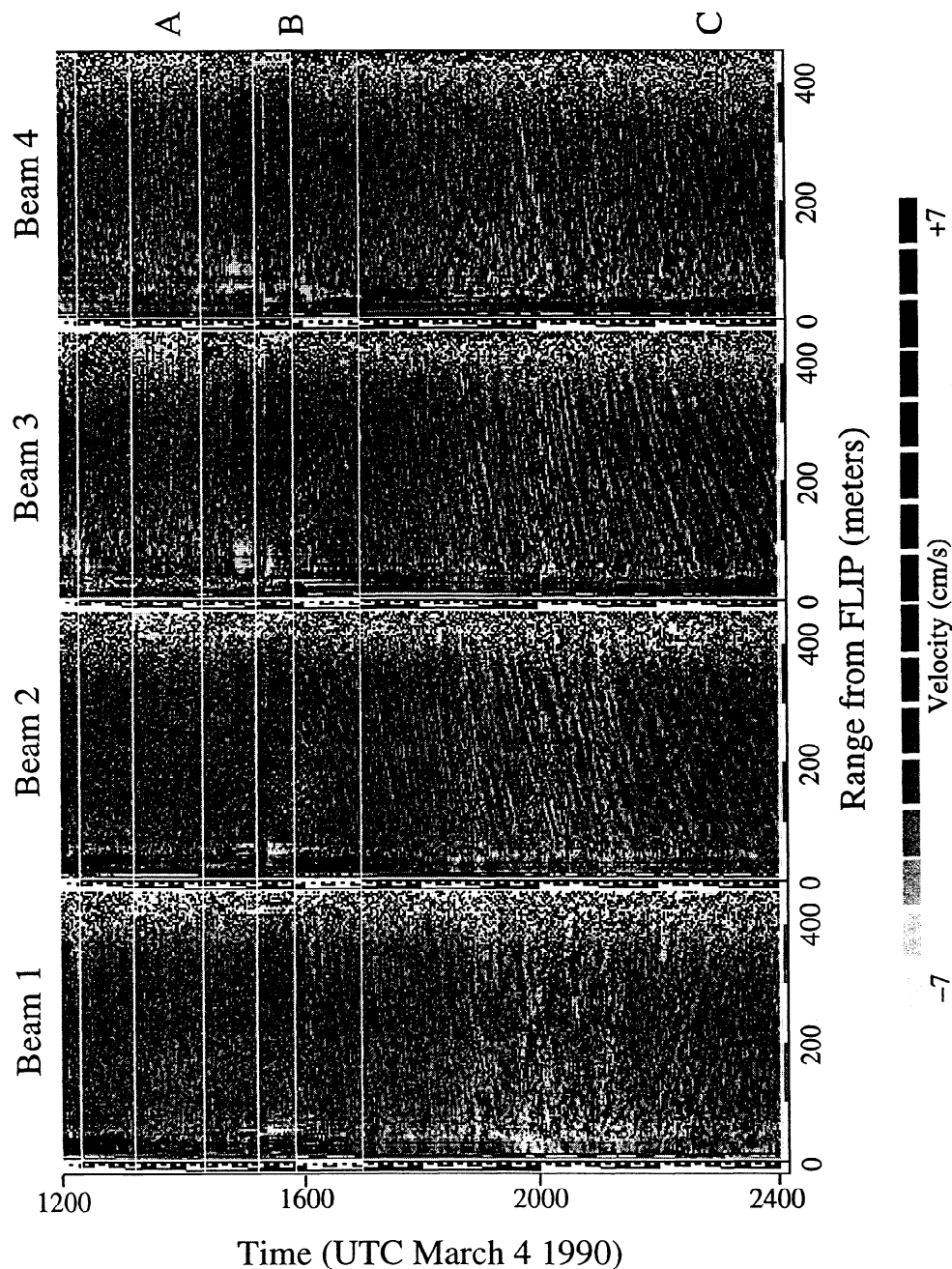
Figure 2a. Time-range maps of Doppler velocity from the four *Flip* sonar beams during the initiation of the second wind event. The data have been averaged over 3 min in time and the range-mean velocity at each time step has been removed. The white lines appearing simultaneously in all beams are data gaps. The sonars do not produce a stable surface return until 40–50 m in range, and beyond about 400 m range the return decays into noise. From 50 to 400-m range the sonars sense convergent and divergent surface velocities due to Langmuir circulation.

after about 2200 UTC (labeled C). Note that the signals are most robust in beams 2 and 3, which were most nearly crosswind during this period, and weaker in beams 1 and 4, which were directed nearly downwind.

The continuous records of backscattered intensity and Doppler velocity from the *Flip* sonars were used to form a subjective index of the existence and strength of circulation patterns. The sonar records were examined

in 1-hour sections for evidence of banded structures; if evident, the degree of contrast and spacing of the bands was noted. A (subjective) numeric scale between −1 and 6 was devised, where −1 meant no data were available, 0 meant data were available but no banded structures were detected, and values from 1 to 6 represented a range of structures progressing from faint, small bands to high-contrast, large-scale bands. Fig-
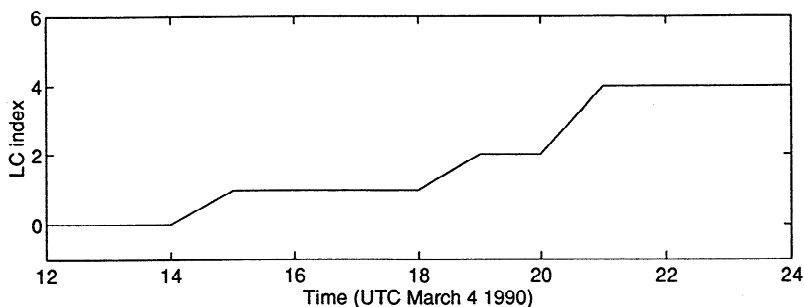
Figure 2b. The subjective Langmuir circulation index during initiation of the second wind event. The index is based on evaluation of convergence zone spacing and strength in the sonar time-range maps. Larger values of the index correspond to more persistent, widely spaced, and stronger convergences.

ure 2b shows the the values of the index during the initiation of the second wind event. The complete record is presented, along with other indices of Langmuir circulation strength, in section 4.1.

An example of a time-range intensity map from the IOS drifter Susy is shown in Figure 3a. The slope of the bands indicates that the cells are being advected away from the instrument at a rate of about 15 cm s^{-1} dur-
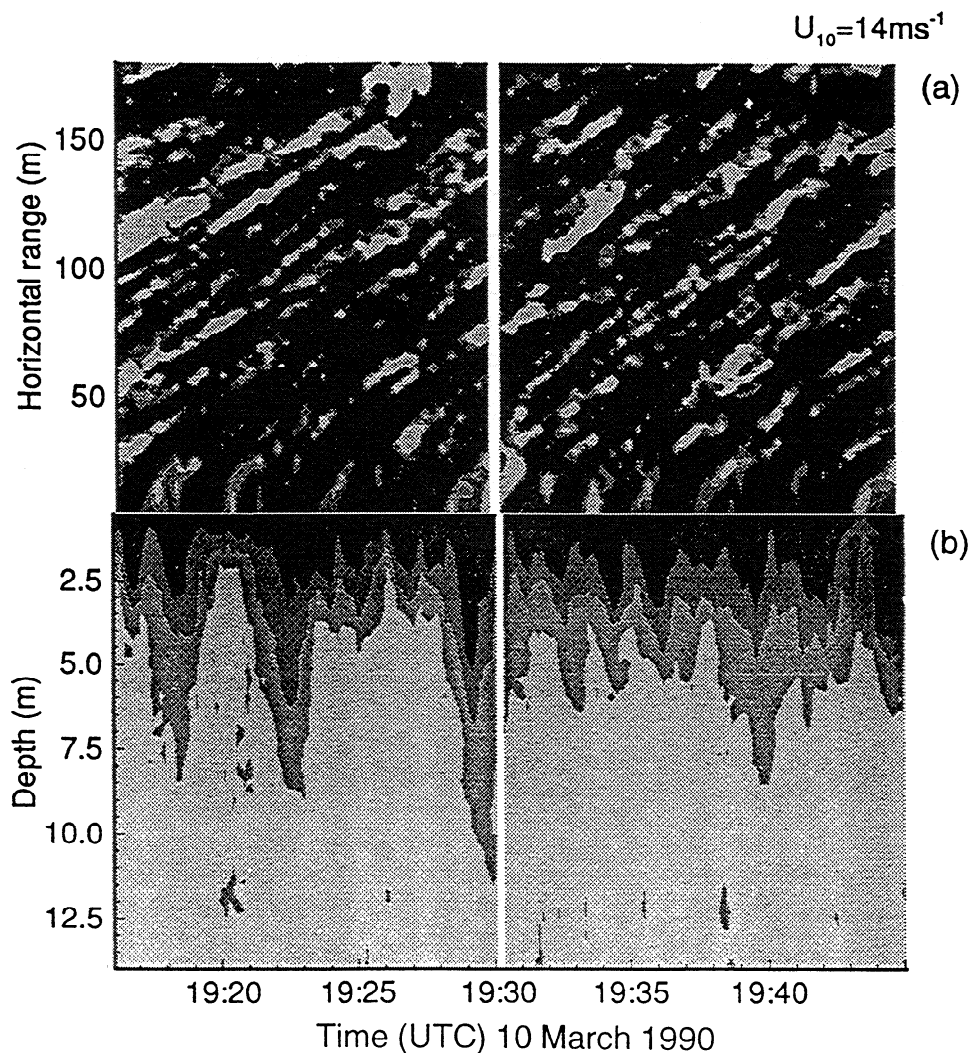

Figure 3. Simultaneous surface-scanning and vertical sonar intensity images from the acoustics drifter "Susy" on March 10. (a) The surface-scan image shows banded structures associated with bubble clouds drawn into rows at Langmuir cell convergence zones. (b) The vertical sonar image shows bubble plumes which penetrate from 2–10 m into the mixed layer. Darker shading indicates higher intensity.

ing this period. A concurrent image of the near-surface bubble layer, based on the target strength of the 50-kHz vertical sonar as a function of depth, is shown in Figure 3b. Target strength measurements were referenced to the sea surface, which therefore appears uniform. The combined image shows that the plumes detected directly above Susy by the vertical sonar typically occur at the same time that the bands in the time-range map are near zero range. Analogous to the results shown by *Zedel and Farmer* [1991], this is evidence that the bands in the surface-scanning sonar image are associated with plumes extending 2–10 m vertically. However, the correspondence is not perfect, and the relationship between the strength of the bands and the strength of the plumes is not well defined.

Figure 4 shows the "skeletonized" bands from two typical surface-scan images at high and low wind speeds.
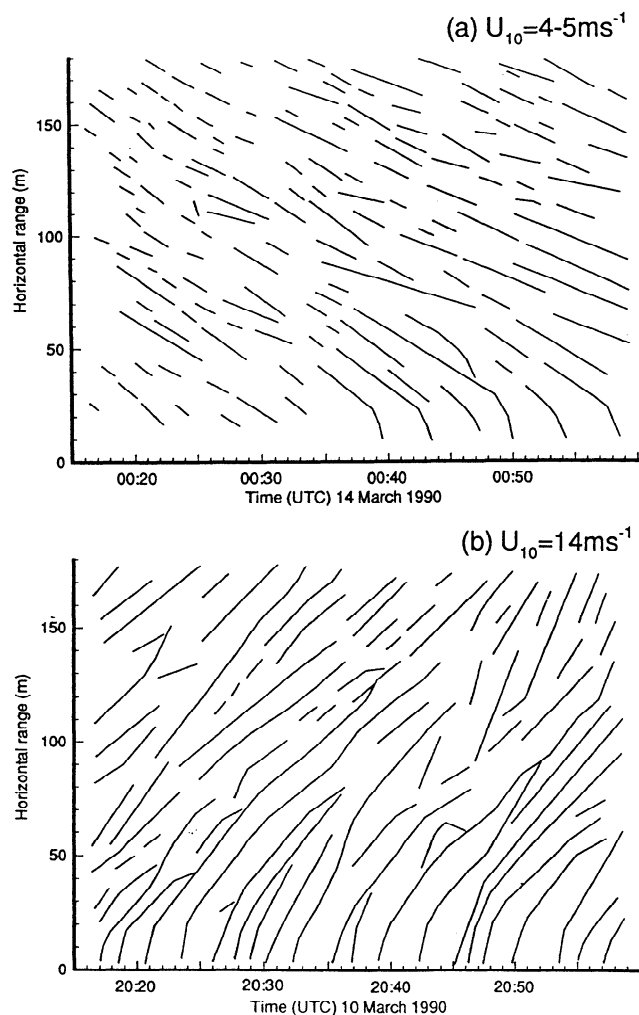

(a) U_{10}=4-5ms^{-1}

Horizontal range (m)

00:20   00:30   00:40   00:50
Time (UTC) 14 March 1990

(b) U_{10}=14ms^{-1}

Horizontal range (m)

20:20   20:30   20:40   20:50
Time (UTC) 10 March 1990

Figure 4. "Skeletonized" bands from two typical surface-scan intensity images at high and low wind speeds. The skeletonized bands for 45-min observation intervals on (a) March 14 and (b) March 10 are shown. The skeletonization process is a subjective visual summary of the time-range maps of intensity (Figure 3a) with lines traced along each clearly distinguishable band of high intensity.
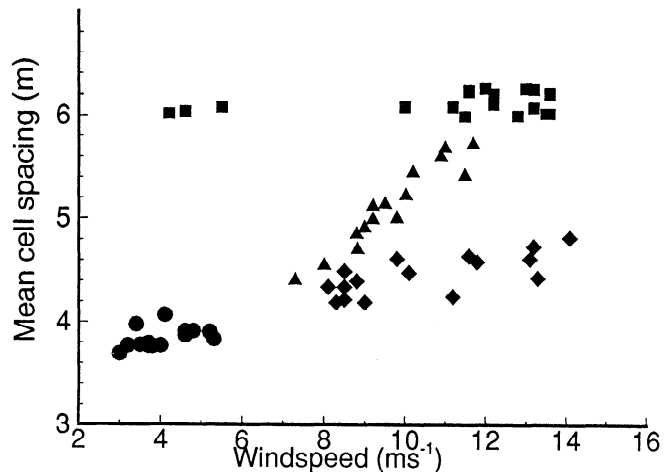

Figure 5. Mean cell spacing versus wind speed from four Susy deployments denoted by different symbols (Table 2). Estimates of cell spacing were made from the skeletonized data by recording the observed spacing versus range at 5-min intervals during each 45-min observation period and assuming that the convergence zones were oriented in the direction of the 45-min average wind. The geometric mean of these estimates was termed the mean cell spacing.

Similar to the "skeleton plots" described by *Thorpe et al.* [1994], these figures are a subjective, visual summary of the time-range maps, with lines traced along each clearly distinguishable band of high intensity. During the time period shown in Figure 4a the wind speed increased from 4 to 5 m s^{-1}. In Figure 4b the wind speed exceeded 13 m s^{-1} but was relatively constant. An obvious difference between the two plots is the temporal persistence of the bands. Even at wind speeds as low as 4 m s^{-1}, there were signs of coherent organization of bubble clouds (Figure 4a, left), but apparently not enough bubbles were present to act as persistent targets and the bands were often discontinuous. As the wind increased toward 5 m s^{-1}, more persistent bands were seen, presumably the result of enhanced bubble production due to increased wave breaking. As the wind speed increased further, the majority of bands were continuous for periods of 5–10 min (Figure 4b).

Earlier observations of Langmuir cells have indicated that the convergence zones are aligned nearly parallel to the wind direction [*Leibovich*, 1983; *Thorpe et al.*, 1985; *Zedel and Farmer*, 1991]. Assuming this to be so, the recorded wind direction from *Flip* was taken as the orientation of the convergence zones, allowing estimation of cell spacing for the Susy deployments. Estimates were made from the skeletonized data by recording the range between intensity bands at 5-min intervals during each 45-min observation period and converting to cross-cell distance using the direction of the 45-min average wind. The geometric mean of these estimates was termed the mean cell spacing. Data from the deployments on March 4–5, March 8–9, March 10, and
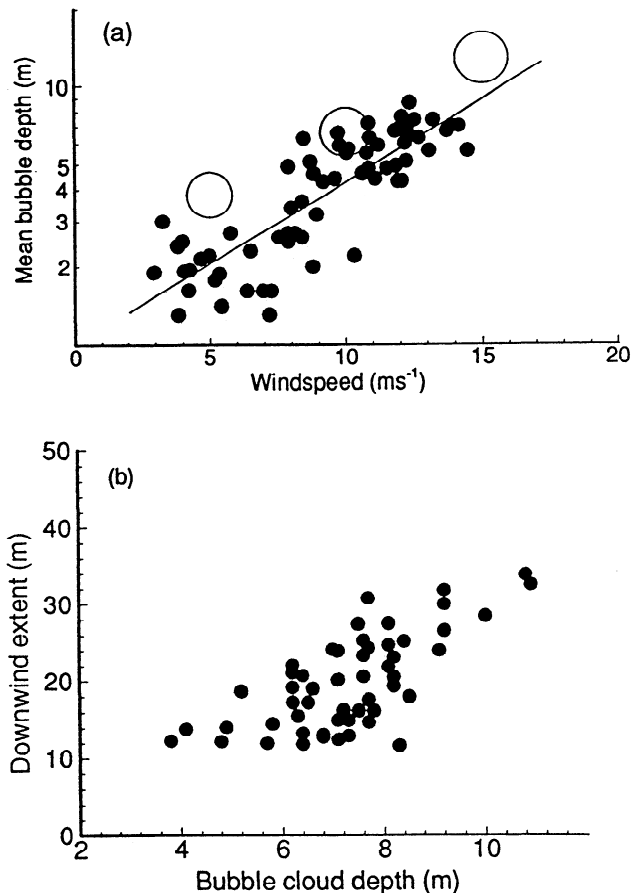
Figure 6. (a) Mean bubble cloud depth versus wind speed for the Susy deployments. The solid line is a least squares fit to the data. The open circles represent similar measurements made by *Thorpe* [1986]. (b) The downwind extent of bubble clouds, estimated from the temporal persistence in time-range maps of Susy surface-scan sonar images, versus bubble cloud depth determined from the vertical sonar.

March 14 showed clearly identifiable bands from which spacing estimates could be made. In Figure 5 the mean cell spacing for each 45-min observation period of the four deployments is plotted against the 45-min average wind speed. There is a tendency for larger cell spacing with higher wind speed; spacing varies from about 3.8 m at 4 m s^{-1} during the March 14 deployment to 6.1 m at 12 m s^{-1} during the March 4–5 deployment, and the spacings from the March 8 deployment fall nicely in between. However, there are also clear departures from this relationship. At the end of the March 4–5 deployment the wind speed dropped rapidly to about 4 m s^{-1}, with no concurrent decrease in cell spacing, and during the March 10 deployment the wind speed increased from approximately 8 to 14 m s^{-1} over a 10-hour period, but the spacing remained nearly constant.

Variations in the depth of the bubble layer were estimated by following the depth of an isopleth of backscattered amplitude from the 88-kHz vertical sonar. The minimum, maximum, and mean penetration depths of the bubble layer were computed over 45-min intervals during each deployment. In Figure 6a the mean bubble cloud depth is plotted against wind speed for the first four deployment periods. Penetration depth increased with increasing wind speed for each deployment. Least squares fits to the data gave $d_{mean} = 1.02\exp(0.14U_{10})$, $d_{min} = 0.42\exp(0.16U_{10})$, and $d_{max} = 2.20\exp(0.13U_{10})$, where U_{10} is the 10-m wind speed. Assuming the bands were oriented approximately downwind, their temporal persistence in the time-range maps was converted to downwind extent (since the component of advection parallel to the bands is ignored, this gives the minimum downwind extent). In Figure 6b the downwind extent of the bubble clouds is plotted against the penetration depth of the same clouds. The downwind extent increases with increasing penetration depth, suggesting that the convergence zones of stronger cells had a longer downwind extent than those of weaker cells. Comparing concurrent estimates of downwind extent and cell spacing showed that the extent was typically 2–3 times the spacing, with little dependence on wind speed.

3.2. Wavenumber Spectra of Sonar Intensity and Velocity

While the investigation of cell structure described in the previous section is revealing, the techniques rely on subjective analysis of the sonar images. The most obvious objective technique for the determination of cell spacing was estimation of the wavenumber spectrum of intensity or velocity versus range. Wavenumber spectra of intensity from Susy and the *Flip* sonars were compared for several common time periods when the beams were oriented nearly crosswind. Figure 7 shows examples from March 5 and 10. The *Flip* sonar had more total range than Susy, while Susy had higher range resolution, thus the differing minimum and maximum wavenumbers in the two spectra. Within the common wavenumber band of the two instruments, the spectra are similar until they begin to "roll off" at high wavenumber. The spectral roll-offs are of similar form for the Susy and *Flip* spectra, and in both cases they begin well below the nominal resolution of the measurement. A possible explanation is that features which were well resolved in range for a single transmission were "smeared" by advective drift along the beam during the several minutes of averaging applied to the data. The spectral roll-offs indicate that wavenumbers above about 0.08 and 0.13 cpm were smeared in the *Flip* and Susy data, respectively.

Within the resolved wavenumber band the most notable property of the spectra is that they are quite flat. The March 5 period was one of well-developed Langmuir circulation, clearly detected by eye in the time-range maps. However, the March 5 spectra in Figure 7a show only very weak indications of a spectral peak (centered near 0.03 cpm). Langmuir cells were weaker on March 10, but still easily detectable in the
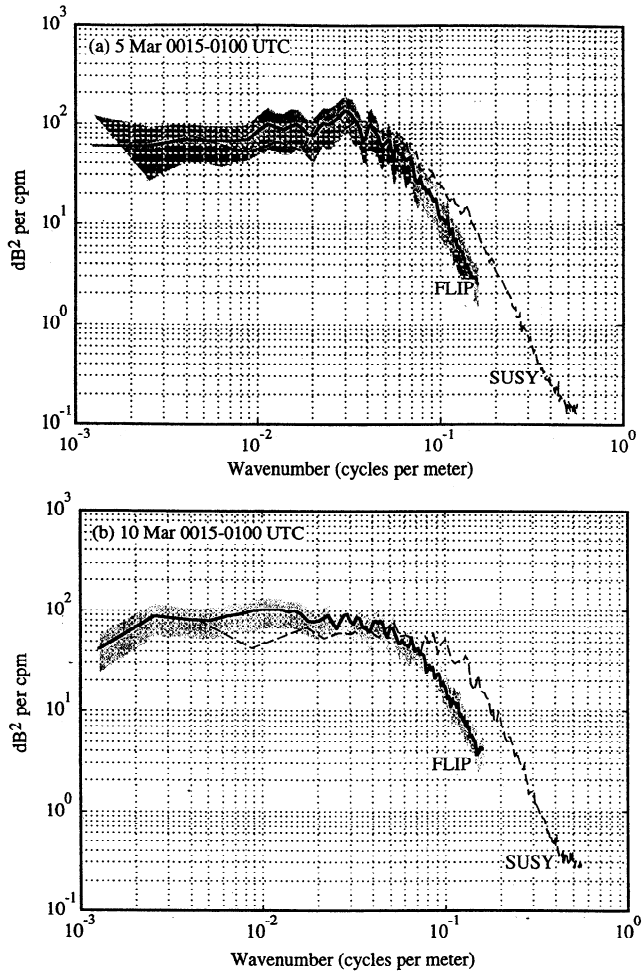
the convergence zone bands. The *Flip* sonars naturally lent themselves to this analysis due to the continuous time-range records and the four available beams, one of which was pointed within 22.5° of crosswind at any time. The 1-min average intensity data $I(r, t)$ for each beam were Fourier transformed in range, giving
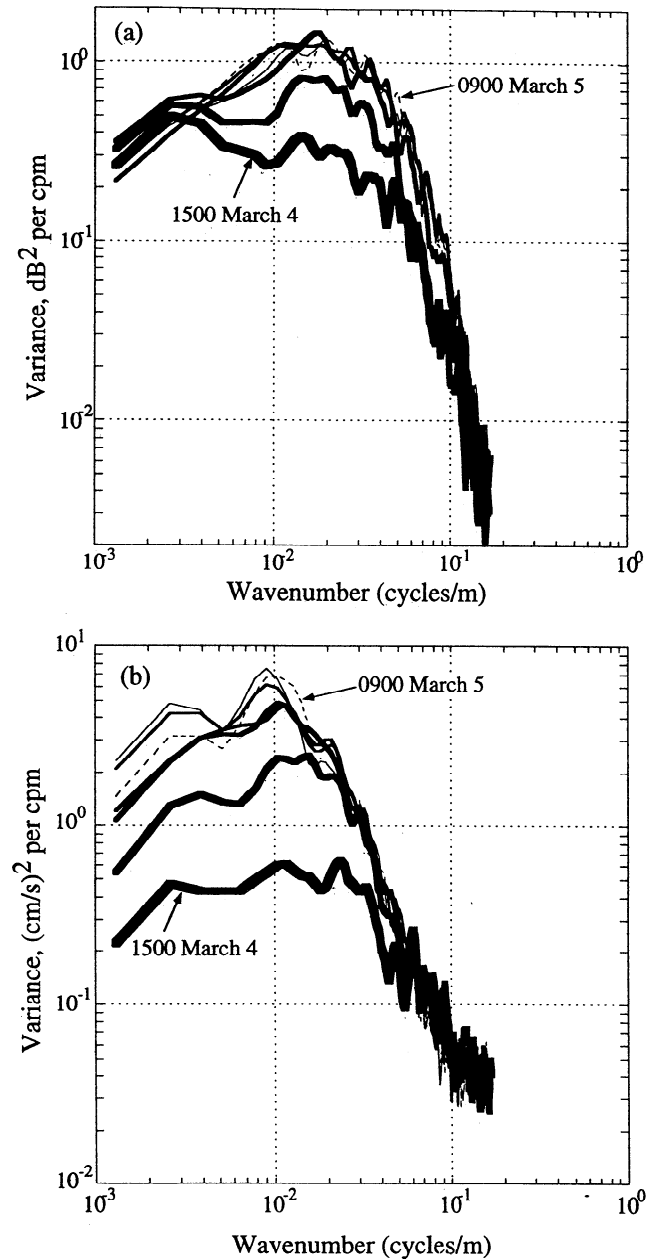
$$A(k, t) = \int I(r, t)e^{-ikr}dr. \qquad (1)$$

Figure 7. Wavenumber spectra of intensity from *Flip* and Susy surface-scanning sonars directed approximately crosswind compared for two time periods: (a) Susy data from 0015 to 0100 UTC on March 5 compared with *Flip* data from the same 45-min period. (b) Susy data from 0015 to 0100 UTC on March 10 compared with *Flip* data from 0141 to 0226 UTC, the nearest common time period. Confidence limits are represented by the shaded area surrounding the *Flip* spectra.

time-range maps. In the presence of this weaker circulation the intensity spectra in Figure 7b fail to show any distinct peaks. Consideration of many spectra like those in Figure 7 for different time periods during SWAPP showed that although the overall energy level changed with time, these spectral shapes were typical.

The lack of peaks in the wavenumber spectra despite the visual impression of evenly spaced bands in the time-range maps of intensity may be due to the natural pattern recognition being done by the human observer. The existence of time-range patterns, which distinguish intensity variance associated with coherent structures, was exploited by including a time lag in the computation of wavenumber spectra. This improves the "signal-to-noise ratio" by suppressing rapidly fluctuating, random "noise" relative to the more persistent "signal" of

Figure 8. Time-lagged wavenumber spectra, analogous to wavenumber autospectra, except for the introduction of a 1-min time lag, from the *Flip* sonar beam directed most nearly crosswind. (a) A sequence of seven intensity spectra presented in 3-hour intervals starting just before the second wind event on March 5. (b) Velocity spectra from the same beam for the same time periods.

The product of the Fourier coefficients at each time with those for 1 min later were then computed and averaged over 1-hour time periods according to

$$C(k, \Delta t) = < A^*(k,t)A(k,t+\Delta t) >, \qquad (2)$$

where $\Delta t = 1$ min, asterisk denotes conjugation, and angle brackets indicate a 1-hour average. The Doppler velocity $V(r,t)$ was processed in the same manner. $C(k, \Delta t)$ is analogous to a wavenumber spectrum, except for the introduction of a time lag. The magnitude of C gives the wavenumber distribution of features which are persistent over a minute or more in time, and the phase is related to the encounter frequency of the features.

A sequence of time-lagged intensity spectra for the beam which was most nearly downwind are presented in Figure 8a at 3-hour intervals, starting from the beginning of the second wind event. The general increase in spectral level during this period of increasing Langmuir circulation strength (Figure 2) is striking (note that there is little variation for wavenumbers above the resolution limit of about 0.1 cpm). The time-lagged processing appears successful in that the spectra are clearly peaked when the circulation is well developed (March 5, 0300-0900 UTC). Still, there is little evidence of "dynamic evolution" or changes in the energy-containing scale with time in these spectra. Energy density increases at about the same rate over a broad range of wavenumbers ($0.005 \leq k \leq 0.1$ cpm) and eventually "saturates" almost simultaneously over the entire range.

The time-lagged velocity spectra from the same beam during the same time period show a noticeably different behavior (Figure 8b). The evolution of the velocity spectra is reminiscent of that for surface waves where high wavenumbers increase first up to a "saturation range" and then remain at a fixed level as lower wavenumbers increase. The result is evolution of the energy-containing scales from small to large as the velocity spectra consistently "peak" near the intersection of a rising low-wavenumber regime and the saturation range. During the period of well-developed circulation a dominant scale near 100 m can be detected. *Smith* [1992] describes the scale evolution during the second wind event in more detail. Of interest here is the interpretation of the scales observed using different techniques, discussed further in section 4.2.

3.3. An Objective Measure of Langmuir Circulation Strength

The apparent dynamic evolution of the time-lagged velocity spectra during a period of cell growth suggested that the signature of evolving Langmuir circulation was being detected and encouraged the use of the velocity data for an objective measure of circulation strength. To the extent that the time-lagged processing selected only the coherent structures in the sonar time-range maps, the velocity variance reflected the strength of the Langmuir circulation. An estimate of this variance could be obtained from the sum over wavenumber of $C(k, \Delta t)$ from (2). However, in order to improve the signal-to-noise ratio in this estimate, further processing steps were introduced to exploit the fact that for short time intervals (1 hour in this case) the Langmuir cells could be considered a "frozen field," advecting past the sonars at a constant speed.

The phase ϕ of the spectral coefficients $C(k, \Delta t)$ at each k is directly related to the frequency of encounter by $\omega(k) = \phi(k)/\Delta t$, as long as $\phi < \pi$ over the interval Δt. For features which were approximately "frozen" into the mixed layer the rate of change of ϕ (and hence ω) with k would be constant. Thus it was advantageous to take the derivative (effectively) of the phase with respect to k by forming the wavenumber-lagged product of the spectral coefficients and then summing these over all wavenumbers:

$$D(\Delta k, \Delta t) =$$
$$\frac{1}{M-1} \sum_{m=1}^{M-1} C^*(k_m, \Delta t)C(k_{m+1}, \Delta t). \qquad (3)$$

The phase of these "double-lagged" spectral coefficients is proportional to the advection speed of features along the beam. To the extent that the frozen field assumption holds, this speed will be constant and the advected features will be summed coherently over all wavenumbers to yield an estimate of the coherent power (from the magnitude of D) and the mean advection speed (from the phase). In practice, the lagged products in (3) were separated into magnitude and phase for each k, and two adjustments were made prior to summing. First, examination of (3) shows that D will have units of $[(cm/s)^2/cpm]^2$, proportional to variance to the fourth power. To recover the more common spectral units of velocity variance density, the square root of the magnitude was taken. Second, it was recognized that the summation in (3) "selects" the variance associated with features traveling at the mean advection speed because they are "inphase." Multiplying the phase by a positive integer has the effect of increasing the suppression of features with advection speeds different from the mean speed. For example, with $\Delta t = 60$ s and $\Delta k = 2\pi/768$ m, "out-of-phase" energy ($\phi = \pi/2$) would have an advection speed 3.2 m s^{-1} different from the mean. This is an unnecessarily large deviation to tolerate, given that typical advection speeds are near 0.2 m s^{-1}, roughly an order of magnitude smaller. Thus the phases of the lagged products in (3) were multiplied by a factor of 4, suppressing advection rates which were different from the mean by more than 0.8 m s^{-1}.

The velocity variance computed from the double-lagged spectral coefficients represents the energy contained in the bands of alternating convergent and divergent velocities seen in the time-range maps (Figure 2), and its square root is referred to as the "rms convergent
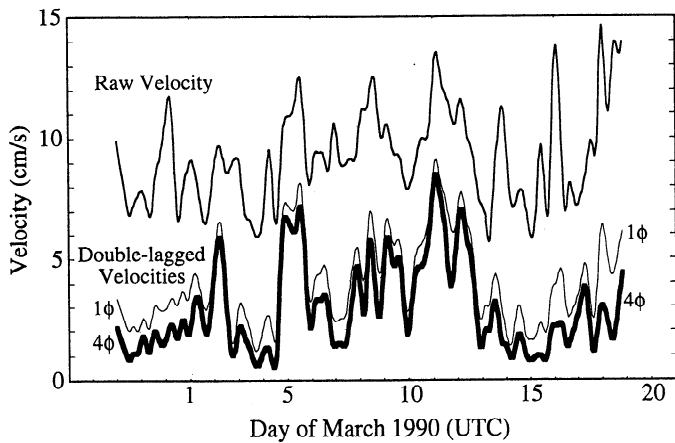
Figure 9. Standard deviation of velocity variance from the double-lagged spectral coefficients (3) compared with the standard deviation of the "raw" Doppler velocities for a single beam. The time and wavenumber lags serve to isolate features which are persistent in time and are advected at a constant speed along the beam. Multiplying the phase ϕ of the cross-spectral product in (3) by a positive integer prior to summation serves to increase the suppression of features with advection speeds different from the mean speed. Double-lagged velocities processed with the phase multiplied by 4 (thick line) are used in subsequent analysis.

velocity." The rms convergent velocity for a single beam is compared to the total velocity in Figure 9. Note that many features in the total velocity are completely absent from the convergent velocity record, and many are

further suppressed by the phase tuning. Rather than attempting to transform the four beams of sonar data into a crosswind and downwind coordinate system, the rms convergent velocity was first computed for each beam separately. Using hourly averages of the wind direction and *Flip*'s heading, the beam most nearly perpendicular with the wind was determined (Figure 10a). A "composite" time series of convergent velocity was then constructed by choosing the value associated with the beam most nearly crosswind for each hour (Figure 10b). This composite record is discussed further in the next section.

4. Discussion

4.1. Variability of Langmuir Circulation Strength

Figure 11 shows the wind stress and wave height during SWAPP, along with three indices of Langmuir circulation strength: the rms convergent velocity from the surface-scanning sonar (described in section 3.3), the band-passed vertical shear from current meters at 2.25 and 6.75 m depth (section 2.2), and a subjective index based on the sonar records (section 3.1). Immediately noticeable is the fact that Langmuir circulation was not a rare occurrence during SWAPP. There are no major discrepancies among the three indices, and all show robust Langmuir circulation associated with the four wind events. The cumulative distribution of the subjective index shows that banded structures were found in the
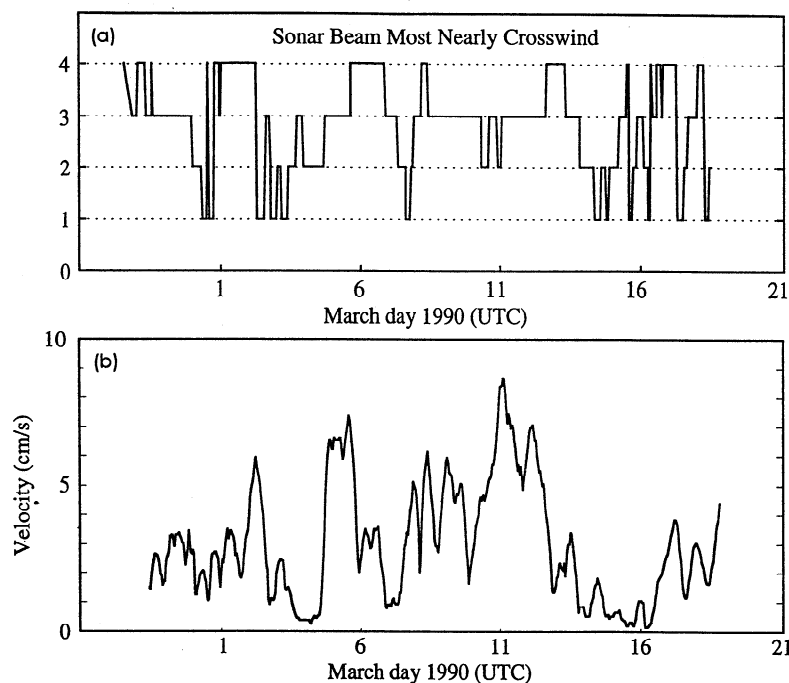

Figure 10. Crosswind velocity variance from the double-lagged spectral coefficients, interpreted as the rms convergent velocity of the Langmuir circulation. (a) The beam most nearly perpendicular with the wind was determined using hourly averages of the wind direction and *Flip*'s heading. (b) The "composite" time series of rms convergent velocity was constructed by choosing the value associated with the crosswind beam for each hour.
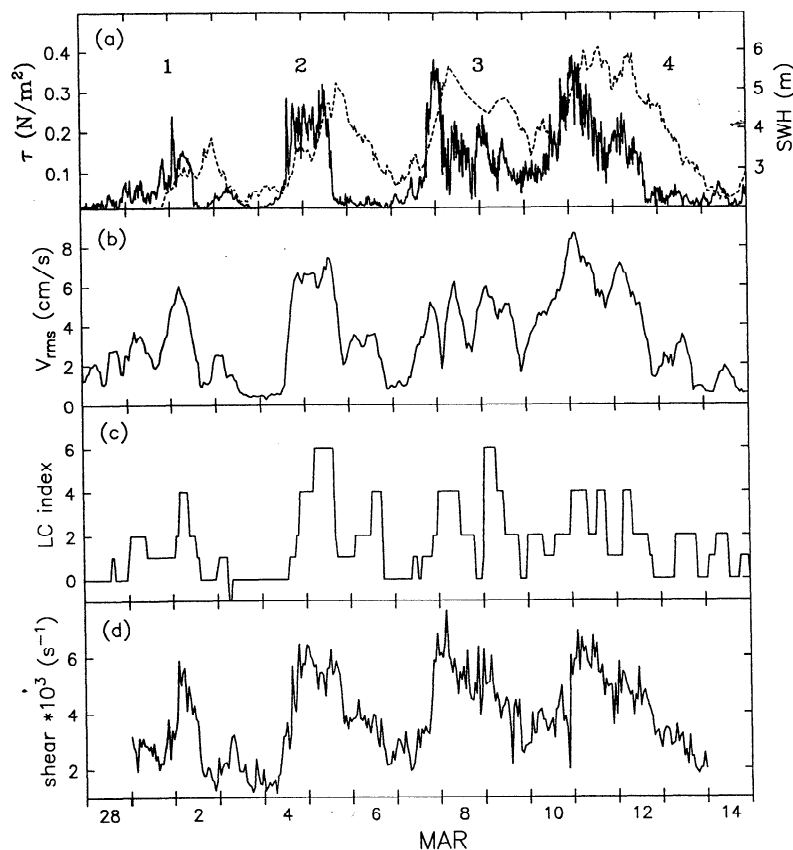
Figure 11. Three indices of Langmuir circulation strength during SWAPP for a time period spanning the first four wind events. (a) Wind stress τ computed using the bulk method of *Large and Pond* [1981], with significant wave height overlaid (dashed line). (b) The rms convergent velocity V_{rms} from the Doppler sonars. This is the "composite" record produced by choosing the value associated with the crosswind sonar beam for each hour. (c) The Langmuir circulation index, derived from a subjective evaluation of convergence zone spacing and strength in the sonar images. (d) The rms 1–36 cph band-passed vertical shear from current meters at 2.25 and 6.75 m depth.

sonar records 60% of the time over 20 days of observations. The rms convergent velocities associated with these structures ranged from a few to over 8 cm s^{-1}. Rms vertical shears of 4–6 $\times 10^{-3}$ s^{-1} were seen during periods of strong circulation.

Attempts to relate the size and strength of Langmuir cells to variations in wind forcing have been made since the work of *Faller and Woodcock* [1964]. Inspection of the variation in wind stress and Langmuir cell strength shown in Figure 11 demonstrates that a simple relationship with wind forcing is unlikely. The indices of Langmuir circulation generally varied in concert with the wind, but there were conspicuous exceptions after the decay of winds associated with the second and fourth events (March 6 and March 13). The second wind event was the most interesting because the onset and decay of the wind was particularly well defined and the presence of Langmuir circulation was indicated by all three indices well after the the wind decayed. Wind growth began at about 0800 UTC on March 4, increasing quickly to about 13 m s^{-1} near 1500 UTC. The wind forcing

decreased abruptly at about 1600 UTC on March 5, but wave height continued to increase, reaching 5.2 m at 1900 UTC before gradually decaying over the next 24 hours. The rms convergent velocity, the subjective index, and the near-surface shear did decrease when the wind dropped, but all remained at levels indicating significant Langmuir circulation until the wave field decayed at about 1900 UTC on March 6. There are two other indications that Langmuir circulation continued after the decrease in wind. First, drifter deployments made on 0145 and 1900 UTC on March 5 both showed relatively fast alignment rates and large row spacings, even though the deployments spanned the drop in wind. Second, the mean cell spacings inferred from time-range maps of intensity (Figure 5) remained near their largest observed values for several hours after the wind speed dropped.

Figure 12a shows the rms convergent velocity V_{rms} during the second wind event versus the friction velocity $u_* = (\tau/\rho)^{1/2}$. The growth and decay phases of this event, identified by different symbols in Figure 12a,

clearly show different behavior. V_{rms} increased from the approximate "noise" threshold of 1 cm s^{-1} to about 6.5 cm s^{-1} as u_* increased from 0.5 to 1.5 cm s^{-1} during the growth phase. However, as expected from the discussion above, V_{rms} did not decrease proportionately when u_* dropped during the decay phase. Values of V_{rms} from 1 to 5 cm s^{-1} were found, while u_* remained relatively steady at about 1.5 cm s^{-1}. The results do not support any simple functional relationship between circulation strength and wind stress. Similar, although less dramatic inconsistencies with wind stress scaling were found for the other events (1 and 4) where a sharp drop in wind speed was followed by gradual decay in wave height.

The inadequacy of the wind stress scaling was presumed to be due to the neglect of surface wave forcing. The presently accepted theory of Langmuir circulation dynamics has been developed from the wave-current interaction theory of *Craik* [1977] and *Leibovich* [1977b] (hereinafter referred to as the Craik-Leibovich theory). In the Craik–Leibovich (CL) theory, Langmuir cells arise from the instability of a sheared mean flow (generally taken to be the wind-driven shear) in the presence of a surface wave Stokes drift. An appropriate scale for the crosswind surface velocity V_{CL} associated with Langmuir circulation is taken from *Leibovich* [1983], written here in terms of the Stokes drift U_s

$$V_{CL} \sim [(L/\nu_e)u_*^2 U_s]^{1/2}. \qquad (4)$$

where L is the wavelength of the dominant surface waves. Eliminating the dependence on the eddy viscosity ν_e is problematic. Very near the surface, ν_e may be influenced by wave breaking [*Agrawal et al.*, 1992], but below this there is some evidence [e.g., *Wu*, 1975; *Leibovich*, 1977a; *Agrawal et al.*, 1992] for the existence of an inertial sublayer, where $\nu_e \sim u_* l_e$. If $l_e = L$ [*Leibovich*, 1977a], then

$$V_{CL} \sim (u_* \, U_s)^{1/2}. \qquad (5)$$

A more general case would introduce a different length scale $l_e = D$ for the eddy viscosity, resulting in a dependence on the ratio $(L/D)^{1/2}$ in (5). If D scales like the surface wave height, (L/D) has the interpretation of an inverse wave slope. Here we assume that the dependence on Stokes drift is of primary importance, equivalent to taking $(L/D) \sim$ constant.

Figure 12b shows the rms convergent velocity for the second wind event versus the Craik–Leibovich scaling (5), with the Stokes drift estimated from the observed wave spectrum [*Kenyon*, 1969; *Huang*, 1971]. Including U_s in the scaling has substantially reduced the scatter and eliminated the discrepancy between the growth and decay phases. The resulting distribution could be reasonably approximated by a linear fit, suggesting that the scaling in (5) properly represents the energetics of the crosswind flow. This scaling was also applied to the other wind events, and a relatively consistent linear re-

lationship was found between V_{rms} and V_{CL} for events 1, 2, and 4 (Figure 13). A linear regression of the form

$$V_{rms} = (-0.4 \pm 0.1) + (2.1 \pm 0.1)V_{CL} \qquad (6)$$

fit the observations with a correlation coefficient of 0.93. Field studies have led several previous investigators to speculate that variation in the wave field must be included in order to correctly describe observed variations in Langmuir cell strength [*Ichiye*, 1967; *Thorpe*, 1986; *Weller and Price*, 1988]. However, we believe that this is the first clear evidence from open ocean observations that the Stokes drift is critical to determining the strength of Langmuir circulation.

The third event was not consistent with either a wind stress scaling or a Craik–Leibovich scaling. Examination of this event shows the limitations of the simple scaling arguments and suggests directions for continued work. In the Craik–Leibovich theory it is assumed that the sheared mean flow $U(z)$ and the Stokes drift are parallel and directed downwind. Examination of the observed near-surface shear shows that these assumptions were generally valid during events 1, 2, and 4. In this case the "vortex force" resulting from cross-stream perturbations in the mean flow shear [*Leibovich*, 1977b, 1983] is a maximum, is destabilizing, and leads to Langmuir circulation. However, there is no restriction in the theory as to the source of the mean shear. In open ocean conditions the actual shear may not be simply the wind-driven shear and may not be parallel to the Stokes drift. Examination of the near-surface shear for event 3 showed that, unlike the other events, there were periods of several hours where the shear was directed nearly upwind and opposite to U_s. In this case the vortex force is stabilizing [*Leibovich*, 1983] and Langmuir circulation is suppressed. Interestingly, these periods (Figure 13, open circles) accounted for the the anomalous points in the distribution of V_{rms} versus V_{CL}. This suggests that although the magnitudes of u_* and U_s provide an effective scaling for Langmuir circulation strength, a more complete analysis requires knowledge of the actual near-surface shear and consideration of its direction relative to the Stokes drift.

4.2. Scales of Langmuir Circulation

Wavenumber spectra of both intensity and velocity (Figure 8) showed increased energy over a broad wavenumber range (10–200 m) during the growth of Langmuir circulation. The spectra rolled off at high wavenumber, indicating that the smallest scales were not resolved. However, surface drifters deployed at the same time that the sonar observations were made showed that smaller scales (2–20 m) were present. Taken together, these results indicated a hierarchy of cell spacings generally consistent with previous dye and drifter deployments [*Katz et al.*, 1965; *Ichiye*, 1967; *Assaf et al.*, 1971; *Weller and Price*, 1988] and sonar observations [*Smith et al.*, 1987; *Thorpe et al.*, 1994]. However,
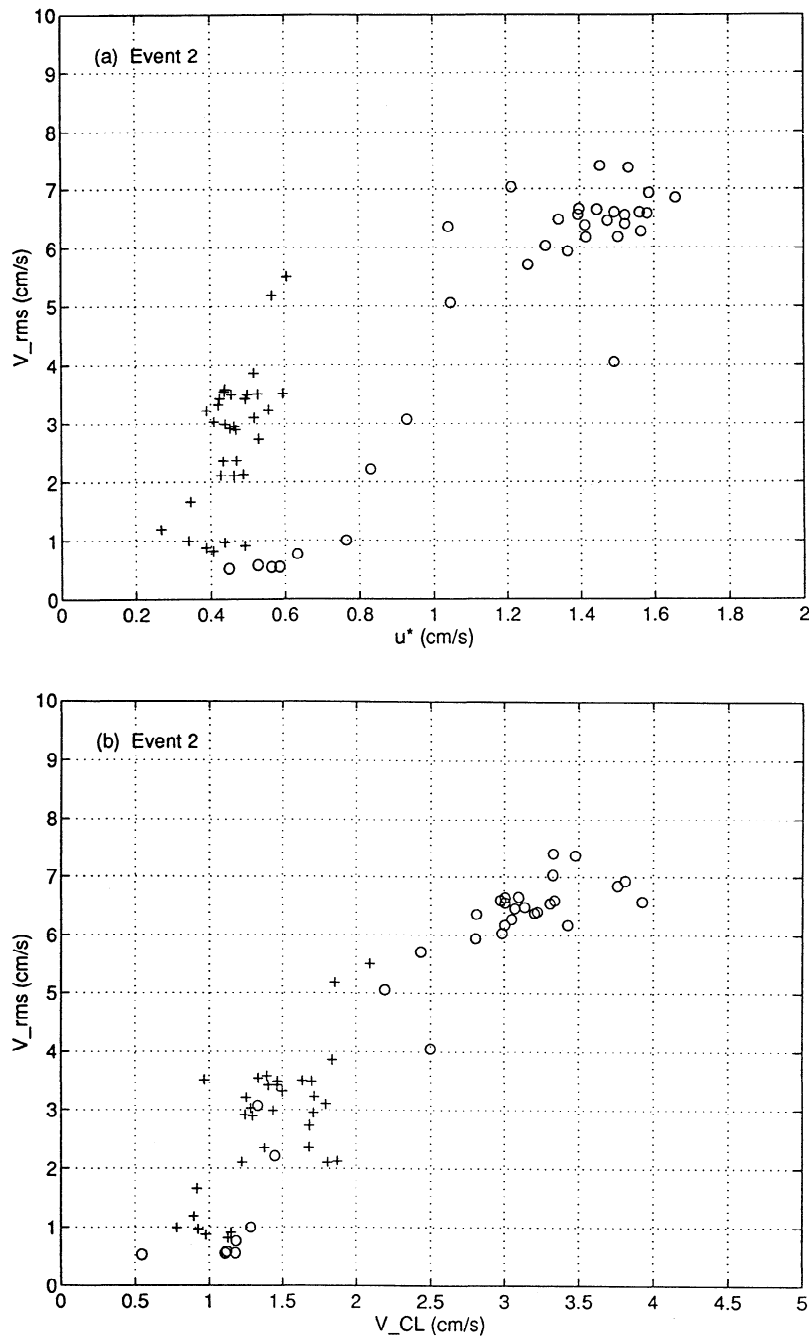
Figure 12. Rms convergent velocity versus surface forcing for the second wind event. Symbols are used to differentiate the wind growth phase (March 4, 0800 UTC, to March 5, 1600 UTC (circles)) from the decay phase (March 5, 1600 UTC, to March 7, 0100 UTC (crosses)). (a) Comparison with $u_* = (\tau/\rho)^{1/2}$ showing no simple relationship. (b) Comparison with the Craik–Leibovich velocity scale $V_{CL} = (u_* U_s)^{1/2}$, where U_s is the Stokes drift, suggesting an approximate linear dependence.

the variety of techniques used simultaneously during SWAPP offered a unique perspective: scales of convergence zone spacing spanning two decades in wavenumber (2–200 m) were consistently present during vigorous Langmuir circulation, but the energy-containing scales evolved in time. The near-surface velocity, which was sensitive to the strength of the circulation, showed this evolution, but other measures of spacing did not. The

key to reconciling this interpretation with the observations lies in an examination of the different methods used to estimate cell spacing.

The surface drifters are quasi-Lagrangian in that they follow horizontal but not vertical motion. *McLeish* [1968] describes how such drifters will initially show the smaller, weaker cells but will eventually be captured in larger, stronger cells. Computer cards deployed
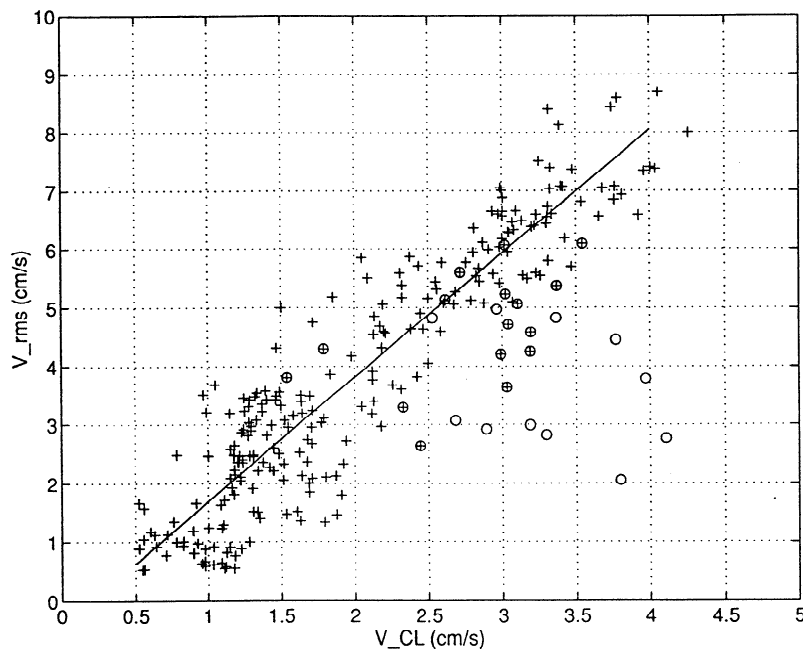
Figure 13. Rms convergent velocity versus the Craik–Leibovich velocity scale for the first four wind events. Events 1, 2, and 4 (crosses) showed a consistent relationship which was well represented by a linear fit (solid line). Significant discrepancies were found for the third event (crossed circles) during times when the near surface shear was not aligned with the wind (open circles).

from *Flip* during conditions favorable for Langmuir cells showed this behavior, initially organizing into rows with spacing of a few meters and later collecting into more widely spaced rows. Reseeding of the surface, after a stable pattern of widely spaced rows was developed, showed that the small-scale cells were still present. Inability to disperse the cards widely in the crosswind direction limited the maximum row spacing detectable from the *Flip* deployments to 15–20 m. However, drifter deployments made from *Parizeau* and *Slicker*, designed to overcome this dispersal limitation, showed spacings of up to 100 m during the same periods that the *Flip* deployments showed 15–20 m spacing. The observations are completely consistent with *McLeish*'s [1968, p. 465] description: "Surface patterns of different scales are thus dominant at different times, and ... only a restricted range of scales appears at any one time."

The microbubbles sensed by the surface-scanning sonars are also quasi-Lagrangian tracers. In addition to being concentrated into "bands" by horizontal convergences, the bubbles can be drawn downward into "plumes" by vertical currents. However, the penetration depth is limited by the fact that the bubbles go into solution at a depth of about 10 m. One method of determining cell spacing from the intensity time-range maps is the skeletonization technique, where a line is drawn for each identifiable band. Since each band is given equal weight, regardless of intensity level, the smallest resolvable scales are emphasized. Indeed, the mean cell spacing over 45-min intervals from skeletonized time-

range maps varied only between 4 and 6 m for wind speeds from 3 to 14 m s^{-1} (Figure 5). Although unaveraged cell spacings of up to 15 m were recorded, these estimates never approached the largest scales observed in the intensity and velocity wavenumber spectra during the same time periods. Modifications to the acoustics drifter since the SWAPP experiment to include azimuthal scanning and Doppler capabilities [*Farmer et al.*, 1995] have revealed three-dimensional features of Langmuir circulation associated with cell merging [*Farmer and Li*, 1995]. Similar features were presumably present during SWAPP and may have been responsible for some of the limitations of the skeletonizaton technique.

Wavenumber spectra of intensity are an objective method of determining cell spacing from the time-range maps which retains sensitivity to the intensity level. However, this may not be sufficient to detect the strength of the circulation. Stronger circulation presumably brings more bubbles per unit time into the convergence zones, but at some point, submergence and dissolution may limit the concentration of bubbles and preclude a direct correspondence between circulation strength and backscattered intensity. The result is that although the time-lagged wavenumber spectra (Figure 8a) show a wider range of scales than the skeletonization technique, indications of scale evolution in time are very weak. Instead, the energy in all scales from about 10 to 200 m rises nearly proportionately as the strength of the Langmuir circulation increases.

The Doppler velocity detected by the sonars does not have the limitations of the intensity-based techniques since circulation strength, in the form of near-surface convergences, is observed directly. Time-lagged wavenumber spectra of velocity show that the energy containing scales do evolve and that a dominant scale may be detected when the circulation is well developed (Figure 8b and *Smith* [1992]). The results also prompt a cautionary note: estimates of cell spacing from any single technique may be misinterpreted if the complete range of cell sizes is not appreciated. For example, during the second wind event the relatively small scales determined from the skeletonized intensity records differed by about a factor of 20 from the largest scales observed in the velocity wavenumber spectra. The large scales were related to mixed layer depth [*Smith*, 1992], but the small scales were not. A related concern is that analytical or numerical models which represent Langmuir circulation using a single scale may not be an appropriate simulation of open ocean conditions.

4.3. Near-Surface Dissipation and Langmuir Circulation

It was our hypothesis that enhanced dissipation rates would be observed in the convergence zones beneath computer card rows due to turbulence production there in the presence of downwelling velocities. This issue was addressed, in part, by the microstructure profiles made at a series of positions relative to the convergence zones (defined by computer card rows) from the launch *Slicker*. The best sets of observations were on March 12 (2147–2358 UTC), when winds were 6–8 m s^{-1} and the swell was about 2–3 m, and March 16 (2209–2341 UTC), when winds were 7–9 m s^{-1} with gusts to 11 m s^{-1}.

Table 3. Dissipation Measurements on March 12

Depth, m	Percent of Row Spacing				
	0–7%	7–12%	12–25%	25–37%	37–50%
5	54.0	69.1	109.1	395.0	60.4
8	43.5	41.2	21.7	31.1	54.9
11	32.0	26.4	24.5	39.7	19.8
15	4.5	4.1	14.5	5.9	20.1
18	1.3	1.9	2.7	2.9	1.2
21	1.0	0.3	0.4	0.2	0.1
25	0.5	0.4	0	0.2	0.1
29	0.8	0.1	0	0	0
32	0	0.1	1.4	0.5	0
36	0	0.1	0	0	0
40	0.8	0.4	0	0	0
44	0.3	0	0	0.2	0
Number of Profiles	7	4	2	6	3

The average dissipation rate ($\times 10^9$ m^2 s^{-3}) is shown for five "range bins" representing increasing horizontal distance from Langmuir cell convergence zones. Dissipation rates below the noise level of the profiler were reported as zero. The number of profiles in each bin is listed at the bottom.

Table 4. Dissipation Measurements on March 16

Depth, m	Percent of Row Spacing			
	0–10%	10–20%	20–35%	35–50%
4	168.8	280.7	65.1	237.5
7	95.5	93.5	69.0	86.2
11	78.2	22.7	54.3	81.8
15	23.5	6.8	35.9	67.4
18	15.0	6.5	33.6	42.7
21	34.3	2.9	27.8	24.9
25	7.4	0	9.5	7.8
29	3.1	0	4.6	0
32	0	0	0.5	0.6
36	0	0	0	0.3
39	0	0	0	0
43	0	0	0	0
Number of Profiles	4	3	4	2

See Table 3 for explanation.

Tables 3 and 4 present the measured rates of turbulent energy dissipation versus depth and distance from the Langmuir cell convergence zones on these 2 days. The results show no clear evidence of increased dissipation rates beneath the card rows. In Table 3, dissipation rates in the upper 20 m are often larger about 1/3 of the way across the cell than near the convergence zones. In Table 4, dissipation rates from 7 to 29 m depth initially drop as the distance from the card rows increases, but rates at 1/4 to 1/2 the row spacing are often greater than those under the rows.

The number of profiles in each horizontal bin was relatively small, and the limitation to modest wind and sea state conditions meant that these profiles were taken during periods of modest Langmuir circulation strength. The rms convergent velocity indicated that the circulation was decaying during the March 12 sampling period and was not strongly developed during the March 16 period. Still, the computer cards formed into clearly defined rows, and the lack of any signal associated with the convergence zones in the dissipation profiles is puzzling. The multiplicity of scales of cells present at any one time may result in a near-surface turbulence layer which, much like the bubble layer (Figure 3b), is highly variable in space and time, without a clear correspondence between strong convergence zones and isolated plumes of deeply penetrating turbulence. More conclusive results may be found if near-surface microstructure profiling can be conducted in higher wind, higher sea state conditions associated with more vigorous Langmuir circulation.

5. Summary and Conclusions

One of the principal results of the paper was the development of an objective measure of Langmuir circulation strength. A processing technique which introduced both time and wavenumber lags in the computation of

velocity variance from a surface-scanning Doppler sonar was introduced. This technique served to isolate the velocity signal associated with coherent features evident in the time-range maps from the total velocity in two ways, first by enforcing a 1-min minimum persistence time and second by coherently summing energy which had a constant advection speed along the beam. To the extent that the Langmuir cells gave rise to uniform rows of convergence and divergence which advected past the sonar beam as a "frozen field," the resulting rms convergent velocity reflected the strength of the Langmuir circulation. It should be noted that the processing included a summation over wavenumber so that the full range of Langmuir circulation scales was represented. Rms convergent velocities of 6 to 8 cm s^{-1} were associated with strong Langmuir circulation, compared to noise levels of about 1 cm s^{-1} detected when no circulation was present.

The time series of rms convergent velocity, along with two other indices of Langmuir circulation strength (band-passed vertical shear from near-surface current meters and a subjective index), showed that Langmuir circulation was a common occurrence during the SWAPP experiment. Circulation strength always increased during or immediately after a substantial increase in wind speed. However, low winds did not preclude the existence of Langmuir circulation. The variation of circulation strength was found to be better related to $(u_*U_s)^{1/2}$ than to u_*. This relationship is consistent with the Craik–Leibovich theory of Langmuir cell generation and emphasizes the significant role of the surface wave Stokes drift U_s in determining circulation strength. Surface waves which decayed more slowly than the wind were apparently responsible for maintaining Langmuir circulation for long periods (up to 24 hours) in the absence of significant wind forcing. Discrepancies in the Craik–Leibovich scaling were confined to situations where the assumptions of the theory were violated.

Estimates of Langmuir cell spacing were made from surface drifters, from subjectively analyzed time-range maps of sonar intensity, and from wavenumber spectra of sonar intensity and velocity. It was concluded that a broad range of scales (2–200 m) existed during periods of Langmuir circulation activity and that the energy-containing scales evolved with time. The drifter deployments were appropriate for determining the range of scales but not for observing scale evolution. Subjectively analyzed time-range maps of intensity tended to emphasize the smallest resolved scale and failed to show evolution over the full range of scales. Sonar intensity spectra showed increases in spectral level over a range of scales (10–200 m) during periods of Langmuir circulation activity but showed little evidence of scale evolution. In contrast, the velocity spectra showed evolution from small to large scales during developing Langmuir circulation. This was attributed to the fact that the near-surface convergent velocity was directly related to circulation strength while the intensity-based techniques were not.

References

Agrawal, Y. C., E. A. Terray, M. A. Donelan, P. A. Hwang, A. J. Williams III, W. M. Drennan, K. K. Kahma, and S. A. Kitaigorodskii, Enhanced dissipation of kinetic energy beneath surface waves, *Nature*, *359*, 219 220, 1992.

Assaf, G., R. Gerard, and A. L. Gordon, Some mechanisms of oceanic mixing revealed in aerial photographs, *J. Geophys. Res.*, *76*, 6550–6572, 1971.

Craik, A. D. D., The generation of Langmuir circulations by an instability mechanism, *J. Fluid Mech.*, *81*, 209–223, 1977.

Crawford, G. B., and D. M. Farmer, On the spatial distribution of ocean bubbles, *J. Geophys. Res.*, *92*, 8231–8243, 1987.

Crawford, W. R., Turbulence observations in the Upper Ocean during the Surface Waves Processes Program (SWAPP) in the Northeast Pacific Ocean, *Can. Data Rep. Hydrogr. Ocean Sci. 106*, 165 pp., Inst. of Ocean Sci., Sidney, B.C., Canada, 1992.

Dewey, R. K., W. R. Crawford, A. E. Gargett, and N. S. Oakey, A microstructure instrument for profiling oceanic turbulence in coastal bottom boundary layers, *J. Mar. Res.*, *46*, 77–103, 1987.

Faller, A. J., and A. H. Woodcock, The spacing of windrows of Sargassum in the ocean, *J. Mar. Res.*, *22*, 3617–3633, 1964.

Farmer, D., and M. Li, Patterns of bubble clouds organized by Langmuir circulation, *J. Phys. Oceanogr.*, *25*, 1426–1440, 1995.

Farmer, D. M., E. A. D'Asaro, M. V. Trevorrow, and G. T. Dairiki, Three-dimensional structure in a tidal convergence front, *Cont. Shelf Res*, *15*, 1649–1673, 1995.

Gnanadesikan, A., Dynamics of Langmuir circulation in oceanic surface layers, Ph.D. thesis, Publ. *WHOI-94-23*, 354 pp., Woods Hole Oceanogr. Inst., Woods Hole, Mass., 1994.

Huang, N. E., Derivation of Stokes drift for a deep-water random gravity wave field, *Deep-Sea Res.*, *18*, 255–259, 1971.

Ichiye, T., Upper ocean boundary-layer flow determined by dye diffusion, in Proceedings of the International Symposium on Boundary Layers and Turbulence, *Phys. Fluids*, *10*, Suppl., 5270–5277, 1967.

Katz, B., R. Gerard, and M. Costin, Response of dye tracers to sea surface conditions, *J. Geophys. Res.*, *70*, 5505–5513, 1965.

Kenyon, K. E., Stokes drift for random gravity waves, *J. Geophys. Res.*, *74*, 6991–6994, 1969.

Langmuir, I., Surface motion of water induced by wind, *Science*, *87*, 119–123, 1938.

Large, W. G., and S. Pond, Open ocean momentum flux measurements in moderate to strong winds, *J. Phys. Oceanogr.*, *11*, 324–336, 1981.

Large, W. G., and S. Pond, Sensible and latent heat flux measurements over the ocean, *J. Phys. Oceanogr.*, *12*, 464–482, 1982.

Leibovich, S. A., On the evolution of the system of wind drift currents and Langmuir circulations in the ocean, *J. Fluid Mech.*, *79*, 715–743, 1977a.

Leibovich, S. A., Convective instability of stably stratified water in the ocean, *J. Fluid Mech.*, *82*, 561–581, 1977b.

Leibovich, S. A., The form and dynamics of Langmuir circulation, *Annu. Rev. Fluid Mech.*, *15*, 391–427, 1983.

McLeish, W., On the mechanism of wind-slick generation, *Deep Sea Res.*, *15*, 461–469, 1968.

Park, M. M., R. C. Singer, A. J. Plueddemann, and R. A. Weller, High-speed real-time data acquisition for Vector Measuring Current Meters, *IEEE J. Oceanic Eng.*, *16*, 360–367, 1991.

Pinkel, R., and J. A. Smith, Repeat sequence codes for improved performance of Doppler sounders, *J. Atmos. Oceanic Technol.*, *9*, 149–163, 1991.

Smith, J. A., Doppler sonar and surface waves: Range and resolution, *J. Atmos. Oceanic Technol.*, *6*, 680–696, 1989.

Smith, J. A., Observed growth of Langmuir Circulation, *J. Geophys. Res.*, *97*, 5651–5664, 1992.

Smith, J. A., R. Pinkel, and R. A. Weller, Velocity structure in the mixed layer during MILDEX, *J. Phys. Oceanogr.*, *17*, 425–439, 1987.

Thorpe, S. A., The effect of Langmuir circulation on the distribution of submerged bubbles caused by breaking wind waves, *J. Fluid Mech.*, *142*, 151–170, 1984.

Thorpe, S. A., Measurements with an automatically recording inverted echo sounder: ARIES and the bubble clouds, *J. Phys. Oceanogr.*, *16*, 1462–1478, 1986.

Thorpe, S. A., and A. J. Hall, The characteristics of breaking waves, bubble clouds, and near-surface currents observed using side-scan sonar, *Cont. Shelf Res.*, *1*, 353–384, 1983.

Thorpe, S. A., A. J. Hall, A. R. Packwood, and A. R. Stubbs, The use of a towed side-scan sonar to investigate processes near the sea surface, *Cont. Shelf Res.*, *4*, 597–607, 1985.

Thorpe, S. A., M. S. Cure, A. Graham, and A. J. Hall, Sonar observations of Langmuir circulation and estimation of dispersion of floating particles, *J. Atmos. Oceanic Technol.*, *11*, 1273–1294, 1994.

Trevorrow, M. V., and R. C. Teichrob, Self-contained acoustics platforms for probing ocean surface processes, *IEEE J. Oceanic Eng.*, *19*, 483–492, 1994.

Vagle, S., and D. M. Farmer, The measurement of bubble size distributions by acoustical backscatter, *J. Atmos. Oceanic Technol.*, *9*, 630–644, 1992.

Weller, R. A., and J. F. Price, Langmuir circulation within the oceanic mixed layer, *Deep Sea Res., Part A*, *35*, 711–747, 1988.

Weller, R. A., M. A. Donelan, M. G. Briscoe, and N. E. Huang, Riding the crest: A tale of two wave experiments, *Bull. Am. Meteorol. Soc.*, *72*, 163–183, 1991.

Wu, J., Wind-induced drift currents, *J. Fluid Mech.*, *68*, 49–70, 1975.

Zedel, L., and D. M. Farmer, Organized structures in subsurface bubble clouds: Langmuir circulation in the open ocean, *J. Geophys. Res.*, *96*, 8889–8900, 1991.

W. R. Crawford, D. M. Farmer, and S. Vagle, Institute of Ocean Sciences, Sidney, B.C. Canada V8L 4B2.

A. Gnanadesikan, A. J. Plueddemann, and R. A. Weller, Department of Physical Oceanography, Woods Hole Oceanographic Institution, Woods Hole, MA 02543–1541 (e-mail: aplueddemann@whoi.edu).

R. Pinkel and J. A. Smith, Scripps Institution of Oceanography, La Jolla, CA 92093.